A New Model for the Morphology of P3HT/PCBM Organic Photovoltaics from Small-Angle Neutron Scattering: Rivers and Streams

Wen Yin[†] and Mark Dadmun[†,‡,*]

[†]Chemistry Department, University of Tennessee, Knoxville, Tennessee, United States, and [‡]Chemical Sciences Division, Oak Ridge National Laboratory, Oak Ridge, Tennessee, United States

ABSTRACT Organic photovoltaics (OPVs) have attracted increasing interest as a lightweight, low-cost, and easy to process replacement for inorganic solar cells. Moreover, the morphology of the OPV active layer is crucial to its performance, where a bicontinuous, interconnected, phase-separated morphology of pure electron donor and acceptor phases is currently believed to be optimal. In this work, we use neutron scattering to investigate the morphology of a model OPV conjugated polymer bulk heterojunction, poly[3-hexylthiophene] (P3HT), and surface-functionalized fullerene 1-(3-methyloxycarbonyl) propyl(1-phenyl [6,6]) C_{61} (PCBM). These results show that P3HT and PCBM form a homogeneous structure containing crystalline P3HT and an amorphous P3HT/PCBM matrix, up to *ca.* 20 vol % PCBM. At 50 vol % PCBM, the samples exhibit a complex structure containing at least P3HT crystals, PCBM crystals, and a homogeneous mixture of the two. The 20 vol % PCBM samples exhibit behavior consistent with the onset of phase separation after 6 h of thermal annealing at 150 °C, but appear to be miscible at shorter annealing times. This suggests that the miscibility limit of PCBM in P3HT is near 20%. Moreover, for the 50 vol % PCBM sample, the interface roughens under thermal annealing possibly owing to the growth of PCBM crystals. These observations suggest a different morphology than is commonly presented in the literature for optimal bulk heterojunctions. We propose a novel "rivers and streams" morphology to describe this system, which is consistent with these scattering results and previously reported photovoltaic functionality of P3HT/PCBM bulk heterojunctions.

KEYWORDS: organic photovoltaics · nanocomposites · conjugated polymers · neutron scattering · phase behavior

Solar energy is a promising alternative energy source because it is abundant, safe, renewable, and clean. However, the high cost of materials and fabrication of solar cells limits its economic feasibility. Thus, although crystalline silicon (Si) accounts for 90% of industrial PV applications, other materials and fabrication procedures have been investigated with the goal of using less material by adopting a thin film structure, or using less expensive semiconductor materials while retaining or improving performance. For these reasons, organic photovoltaics (OPV) have attracted significant interest as a material to convert sunlight into electricity.[1−8] Organic and polymeric materials are a promising replacement for their inorganic counterparts in photovoltaics due to their low cost, ease of processing, and straightforward thin film formation.

The conversion of solar energy to electricity in an OPV occurs in three consecutive steps: the generation of excitons by absorption, the dissociation of excitons into free charge carriers, and the transport of electrons and holes to the electrodes. Unlike inorganic photovoltaics, the electrons and holes formed upon absorption are bound together as excitons by electrostatic forces in OPV. Subsequently, the dissociation of excitons is most efficient at acceptor−donor heterojunctions (*i.e.*, interfaces). Moreover, the excitons can travel only a short distance (typically ∼100 Å) before they recombine.[9−11] The current understanding of OPVs suggests that bulk heterojunctions composed of phase-separated donor and acceptor materials overcome this shortcoming by forming interpenetrating networks with large donor/acceptor interfacial area (Figure 1A). This structure facilitates both exciton dissociation and charge carrier transport, resulting in energy conversion efficiencies approaching 5−7%.[2,12] Both molecular ordering of the donor/acceptor material and the scale of phase separation are crucial in realizing a structure that can effectively dissociate excitons and transport the charges to the electrodes. There has been significant effort to optimize the morphology of the OPV by manipulating controllable parameters, such as donor/acceptor ratio,[13,14] device processing method,[2,15,16] and postpreparation treatment such as thermal and vapor annealing.[17−19] Despite this uncertainty, optimal

* Address correspondence to Dad@utk.edu.

Received for review February 23, 2011 and accepted May 12, 2011.

Published online May 12, 2011
10.1021/nn200744q

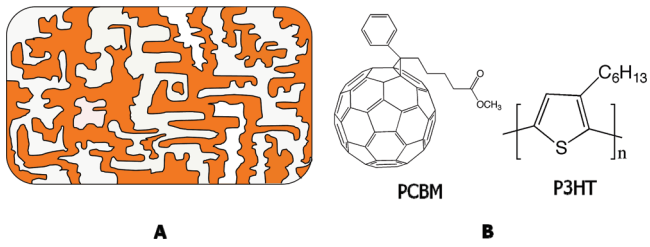

Figure 1. (A) Schematic diagram of the currently believed bulk heterojunctions' morphology, where white domains account for electron donor and orange domains represent electron acceptor. (B) Molecular structures of [6,6]-phenyl C_{61} butyric acid methyl ester (PCBM) and poly(3-hexylthiophene) (P3HT).

efficiencies are often achieved with an acceptor/donor ratio near 1:1, and thermal or solvent annealing is required to enhance conversion efficiency. Many techniques have been applied to correlate morphology and device efficiency including atomic force microscopy (AFM),[8] ellipsometry,[20] transmission electron microscopy (TEM),[21,22] X-ray scattering,[23,24] X-ray reflectivity,[19] and others.[25,26] However, there is limited contrast between the carbon-based conjugated polymer (donor) and carbon nanoparticle fullerene derivatives (acceptor) using an electron-based technique, leading to ambiguity in the interpretation of these results. In particular, differentiating between an amorphous P3HT phase and an amorphous mixture of P3HT and PCBM is very difficult with these techniques. AFM provides information only on the surface, which may not represent the bulk morphology.

Neutron scattering, however, provides unique contrast for this system because the scattering length density (SLD) of fullerene derivatives is significantly different from the protonated conjugated polymer and, hence, provides much more detailed information on their structure, interfaces, and morphology. In this paper, P3HT/PCBM blends (Figure 1B) of varying composition are prepared *via* continuous solvent drop casting and examined using small-angle neutron scattering (SANS). In this study, the P3HT/PCBM samples are thermally annealed at 150 °C for different amounts of time to examine the change in morphology and interfacial structure with thermal annealing. Our SANS results indicate that P3HT/PCBM blends have a very different morphology than that which is usually presented in the OPV literature. This observation is reconciled by proposing a new morphology for the P3HT/PCBM OPV system that agrees with our results and also is consistent with current results in the literature.

RESULTS

The SANS results of a series of PCBM/P3HT blends with 10, 15, 20, and 50 vol % PCBM (denoted PCBM10, PCBM15, PCBM20, and PCBM50, respectively) are presented in Figures 2 and 3. These samples were annealed in a vacuum oven at 150 °C for various times between each measurement to study the impact of thermal annealing on their morphology. Focusing on the high-Q regime first, all plots exhibit peaks at $Q \approx 0.38$ Å^{-1}, corresponding to a d-spacing of 16 Å. This spacing is consistent with the P3HT lamellae D_{100} peak,[23] indicating the presence of P3HT crystals in all samples, and that no PCBM molecules intercalate into the P3HT crystalline structure. On the other hand, only the 50 vol % PCBM blends (PCBM50, Figure 3B) exhibit a clear peak at $Q \approx 0.67$ Å^{-1}, consistent with the crystal peak of pure PCBM.[23]

The qualitative inspection of these scattering curves offers significant insight into the morphology and interfacial structure of these bulk heterojunctions. A noteworthy feature in all SANS patterns is the Porod scattering regime in the range $\sim 0.02 < Q < \sim 0.2$ Å^{-1}, indicative of the presence of an interface. Similar Porod scattering is also observed for neat P3HT (Figure S1), which consists only of crystalline P3HT and amorphous P3HT. The scattering intensity of the pure P3HT sample exhibits much lower absolute intensity, which is a result of significantly lower contrast between crystalline P3HT and amorphous P3HT relative to the P3HT/PCBM samples.

A correlation peak appears at slightly smaller Q ($0.01 < Q < 0.04$ Å^{-1}). At even smaller Q ($Q < 0.01$ Å^{-1}), PCBM50 shows a significant increase in scattering intensity, indicative of the development of a large-scale structure that is absent in the other samples. This low-Q scattering regime in PCBM50, along with the existence of both PCBM and P3HT crystals, indicates that the PCBM50 samples are phase-separated. Conversely, the modest low Q scattering of PCBM10, PCBM15, and PCBM20 indicates that these systems are more homogeneous, where the structure in this concentration regime can be viewed as pure P3HT crystals dispersed in a matrix that is a homogeneous mixture of amorphous P3HT and PCBM. Therefore, the high-Q Porod regimes in these systems correlate to the interface between pure P3HT crystals and this amorphous matrix. Careful inspection of Figure 3A demonstrates that after 6 h of thermal annealing the PCBM20 sample exhibits an upturn in scattering intensity at low Q, indicating the development of a larger scale structure. This behavior is consistent with a system that is influenced by growing concentration fluctuations near the binodal.

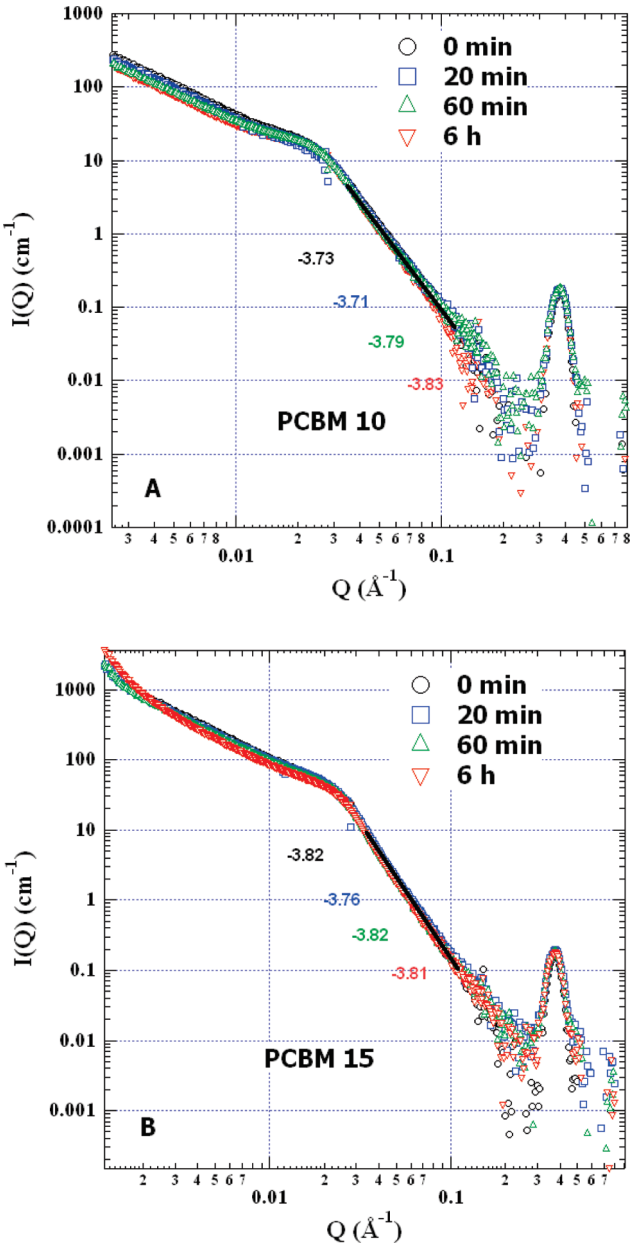

Figure 2. Measured structure factor in absolute intensity of (A) 10 vol % PCBM blend and (B) 15 vol % PCBM blend. The exponents of Porod analysis at high *Q* are also listed.

All Porod regimes are fitted to $I(Q) \approx Q^{-\alpha}$, where α is listed in Table 1 for all samples. For PCBM10, PCBM15, and PCBM20, α stays around 3.75 before and after thermal annealing, indicative of a reasonably sharp, stable interface. However, for PCBM50, α decreases with thermal annealing. α is related to the surface fractal dimension (D_s) as $\alpha = 6 - D_s$, where a value of $\alpha = 4$ is expected for a smooth, sharp, two-dimensional interface. A decrease in α is equivalent to the increase of fractal dimension, which in turn indicates the roughening or broadening of the interface. This is contrary to current models, which imply that thermal annealing after casting results in the increased phase separation of the P3HT and PCBM. This result clearly shows that the interface broadens with thermal annealing, suggesting that there is mixing at the interface, not phase separation, which would result in a sharpening of the interface. This is the first result of this study that suggests the current interconnected, bicontinuous two-phase model for an ideal organic photovoltaic is incorrect.

For PCBM20, α stays relatively constant up to 60 min thermal annealing, then decreases considerably after 6 h thermal annealing. This behavior is consistent with the onset of phase separation in this system, as the α at early times characterizes the P3HT crystal/amorphous interface. However at six hours, the presence of an incipient interface between an amorphous PCBM-rich phase and an amorphous P3HT-rich phase should be broader than the crystal amorphous interface, resulting in a lower α.

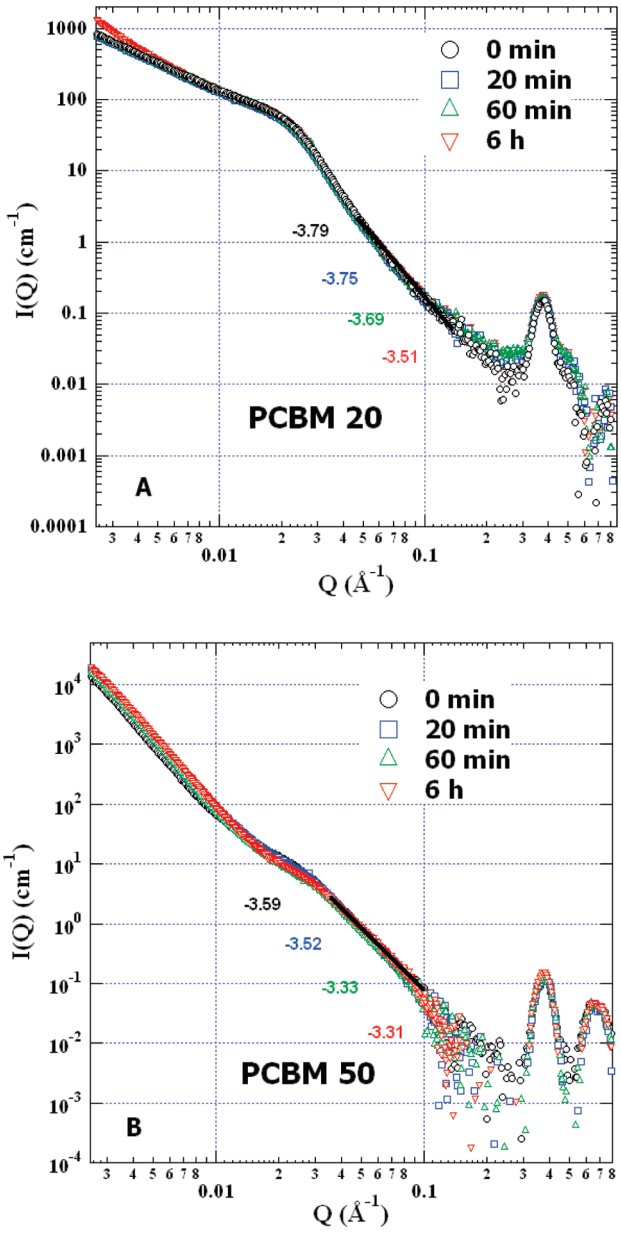

Figure 3. Structure factor in absolute intensity of (A) 20 vol % PCBM blends and (B) 50 vol % PCBM blends after annealing for 0, 20, and 60 min and 6 h at 150 °C. The exponents of Porod analysis at high *Q* are also listed.

TABLE 1. α Obtained from Power Law Fitting of the Porod Scattering Regime in Figure 2

	α			
	PCBM10	PCBM15	PCBM20	PCBM50
0 min	3.73 ± 0.03	3.82 ± 0.03	3.79 ± 0.02	3.59 ± 0.02
20 min	3.71 ± 0.02	3.76 ± 0.01	3.75 ± 0.02	3.52 ± 0.02
60 min	3.79 ± 0.03	3.82 ± 0.02	3.69 ± 0.02	3.33 ± 0.05
6 h	3.83 ± 0.03	3.81 ± 0.02	3.51 ± 0.01	3.31 ± 0.05

Figure 4 shows the Lorentz-corrected scattering of the samples, where Figure 4A focuses on the high-*Q* regime, while Figure 4B focuses on the low-*Q* regime. In Figure 4A, the Lorentz-corrected scattering patterns of the P3HT and PCBM crystal peaks are even clearer. This figure also shows that PCBM20 exhibits slightly more scattering in this *Q* range ($0.6 < Q < 0.8$ Å^{-1}) than PCBM10 and PCBM15.

In Figure 4B, it is clear that PCBM50 exhibits much larger scattering than the other samples in the low-*Q* range, consistent with our conclusion that PCBM50 samples are phase-separated, while the other blends form homogeneous systems. The correlation peaks at $Q \approx 0.02$ Å^{-1} correspond to the long period of P3HT lamellae crystals, which is the mean average distance between lamellae domains, including the length of the P3HT crystals and the amorphous domains between these crystals.[27] These peaks are clear in the 10, 15, and 20 vol % PCBM samples and are less well-defined in

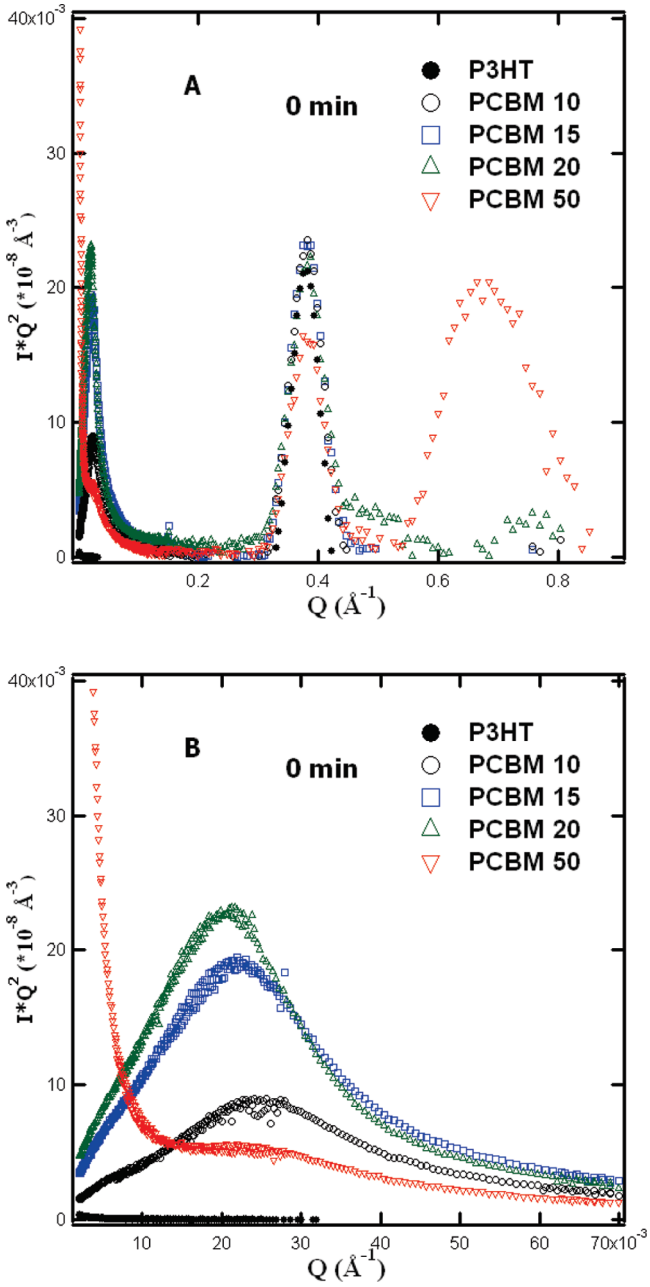

Figure 4. (A) Lorentz-corrected scattering pattern for the as-cast films of neat P3HT and 10, 15, 20, and 50 vol % PCBM blends in P3HT. (B) Low-*Q* amplification of the Lorentz-corrected scattering pattern presented in A.

PCBM50, possibly due to the existence of PCBM crystals. One interesting feature here is that this peak is absent for neat P3HT, potentially due to the limited contrast between crystalline and amorphous P3HT. However, in the blends samples, this contrast is greatly enhanced by the incorporation of PCBM into the amorphous P3HT. Hence, the correlation peak is clearly present and grows in height with percent PCBM in the homogeneous regime, further supporting the interpretation that the morphology of these samples is P3HT crystals dispersed homogenously in the mixture of amorphous PCBM and P3HT.

Additional quantification supports this interpretation further, where in Table 2, the peak position and the corresponding long period ($2\pi/Q_m$) of the samples are presented. The long period increases when the % PCBM increases from 10 to 20 vol %, indicating the distance between P3HT crystals is increasing. This is consistent with the mixing of additional PCBM into the

TABLE 2. *Q* Value and the Corresponding P3HT Crystal Long Period (*L*) Calculated from the Correlation Peaks in the Lorentz-Corrected Scattering Pattern

	PCBM10	PCBM15	PCBM20	PCBM50
Q_{max} (Å^{-1})	0.0250	0.0209	0.0202	0.0219
L (Å)	251	301	311	287

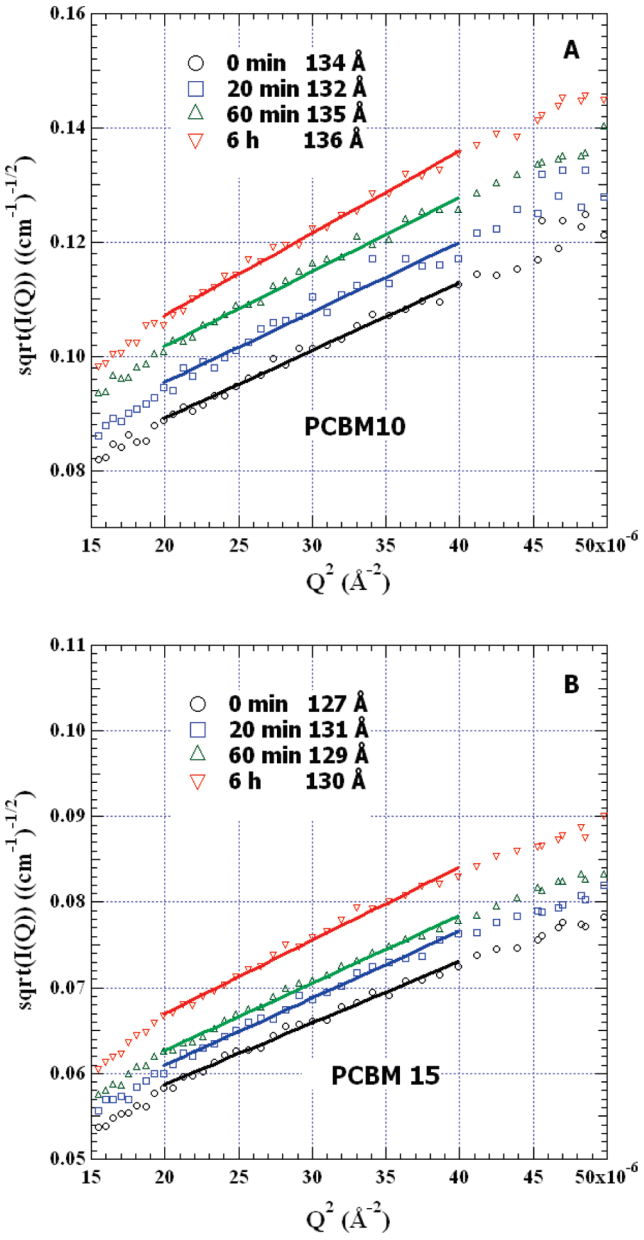

Figure 5. Debye−Bueche fits of (A) 10 vol % PCBM and (B) 15 vol % PCBM, for thermal annealing at 150 °C for 0, 20, and 60 min and 6 h.

amorphous phase upon its addition to the sample, further separating the existing P3HT crystals. However, the long period of P3HT crystals of PCBM50 decreases relative to the PCBM20 sample with its additional PCBM, indicating that this PCBM phase separates into a third phase and does not lie in the amorphous phase between the crystals. Furthermore, a preliminary SANS study of a 25 vol % PCBM sample (PCBM25) indicates that the correlation peak of the as-cast PCBM25 sample is shifted to a larger Q than that of PCBM20, yielding a smaller long period. (Supporting Information Figure S2 and Table S1) This implies that the additional PCBM does not mix between the crystals, further strengthening the interpretation that the miscibility limit between P3HT and PCBM is near 20 vol %.

Further quantitative analysis of these scattering curves provides supplementary insight into the structure of these mixtures, as well as verification of the model presented. Pursuant to this, the size of the domains that give rise to the scattering was analyzed by fitting the structure factor to the Debye−Bueche equation for all blend samples:[28,29]

$$I(Q) = I_0/(1+Q^2\xi^2)^2$$

In this equation, ξ is the correlation length and I_0 the zero-angle scattering intensity. This analysis is shown in Figures 5 and 6, which plots $I(Q)^{-1/2}$ as a function of Q^2 for all samples. The corresponding correlation lengths ξ are listed in Table 3. The correlation lengths for the 10, 15, and 20 vol % PCBM samples are relatively

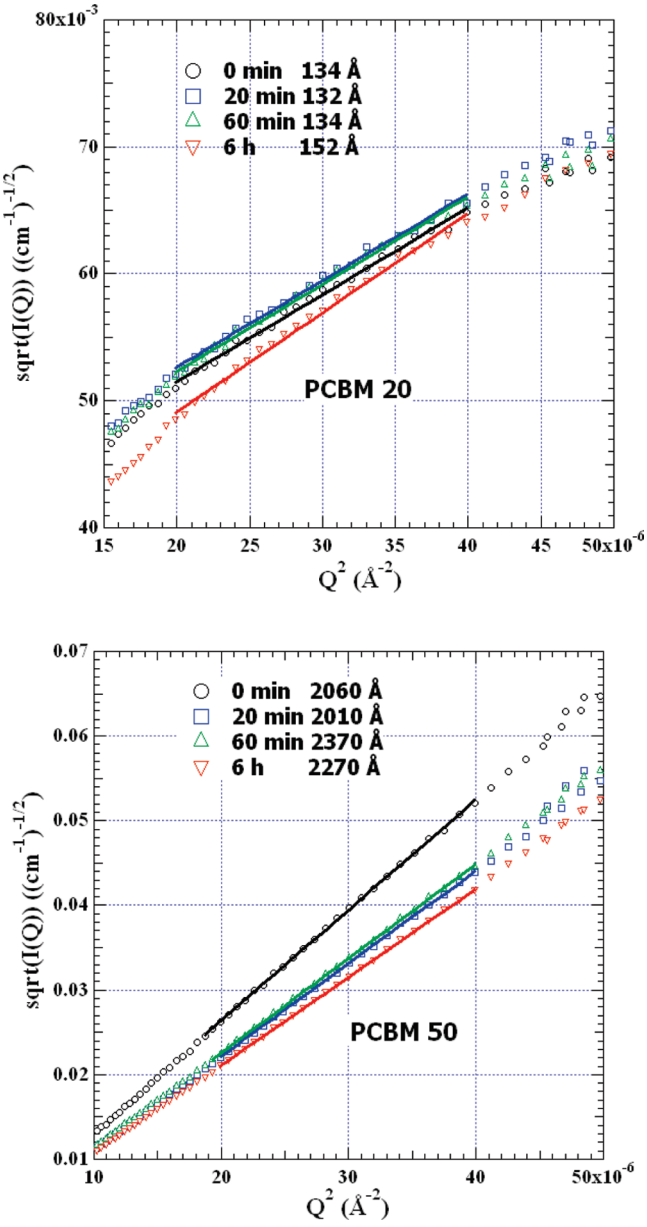

Figure 6. Debye–Bueche fits of (A) 20 vol % PCBM and (B) 50 vol % PCBM, for annealing at 150 °C for 0, 20, and 60 min and 6 h.

constant, remaining 130–135 Å, even with extended annealing at 150 °C, except for the PCBM20 sample at the longest annealing time. As the scattering contrast in these samples comes from the pure P3HT crystals that are dispersed in an amorphous homogeneous PCBM/P3HT matrix, these results indicate that the size of the P3HT crystals does not change in these samples with annealing. The increased correlation length of PCBM20 after 6 h is consistent with the inception of phase separation, forming additional long-range structures, presumably a PCBM-rich phase, that are larger than the P3HT crystals.

The PCBM50 sample, however, exhibits much larger correlation lengths, greater than 2000 Å. This is not surprising, as there exist additional structures in this sample that are not in the PCBM10, PCBM15, or PCBM20 samples, including PCBM crystals, which clearly dominate the correlation length. An increase in the P3HT crystal size could also result in this increased correlation length; however, the results presented in Table 2

TABLE 3. Correlation Lengths Obtained from Debye–Bueche Fitting the Low-*Q* Regime of the Absolute Scattering Pattern

	correlation length (Å)			
	PCBM10	PCBM15	PCBM20	PCBM50
0 min	134 ± 2	127 ± 2	134 ± 2	2060 ± 30
20 min	132 ± 3	131 ± 2	132 ± 2	2010 ± 20
60 min	135 ± 3	129 ± 1	134 ± 1	2370 ± 50
6 h	136 ± 3	130 ± 2	152 ± 4	2270 ± 40

TABLE 4. Length Scale of Heterogeneity for the P3HT/PCBM Samples As a Function of Thermal Annealing Time at 150 °C As Determined by Porod Analysis

	l_p (Å)			
	PCBM10	PCBM15	PCBM20	PCBM50
0 min	99 ± 3	124 ± 7	170 ± 10	190 ± 20
20 min	114 ± 3	140 ± 8	190 ± 10	240 ± 20
60 min	119 ± 4	140 ± 8	160 ± 10	230 ± 20
6 h	109 ± 3	132 ± 8	160 ± 10	160 ± 10

show no significant growth of the P3HT crystals, nor does the Scherrer analysis of the P3HT crystal peak presented below. Therefore, the increase in ξ is indicative of the onset of macroscopic phase separation in this sample, unlike in the samples with lower loadings of PCBM.

Finally, Porod analysis of the two-phase structure can also provide insight into the length scale of heterogeneity in these samples. In this analysis $\ln(IQ^4)$ is plotted as a function of Q^2 (Figure S3), where the length scale of heterogeneity, l_p, in the system is then extracted from the slope and invariant (Figure S4).[27,30] More precisely, in a Q^4I_{obs} *vs* Q^2 plot, the intercept is $k/2\pi^3l_p$ and the slope is $-2k\sigma^2/\pi l_p$, k comes from the invariant, and thus l_p can be determined from the intercept.

The length scale of heterogeneity, l_p, that is calculated from this analysis is shown in Table 4. These values are consistent with the Debye–Bueche and P3HT long period analysis provided above, showing that the length scale of the heterogeneity is between 100 and 200 Å for the PCBM10, PCBM15, and PCBM20 samples. The length scale of heterogeneity increases significantly for the PCBM50 sample, presumably due to the macroscopic phase separation. It is surprising, however, that l_p does not increase more, given its large correlation length in Table 3. This lack of quantitative agreement between the Porod analysis and the correlation length and long period determination, however, can be explained and lies in the definition of l_p. For a two-phase structure

$$\frac{1}{l_p} = \frac{1}{l_1} + \frac{1}{l_2} \qquad (2)$$

where l_1 is the length scale of phase 1 and l_2 is the length scale of phase 2.[31] Therefore, l_p is dominated by the smaller phase, while the contribution of the larger phase (PCBM crystals in PCBM50) to l_p is nominal. This results in a measured l_p that is closer to the size of the smaller phase than the larger phase, as is observed in these results.

Therefore, the analyses presented above are consistent with a picture of the P3HT/PCBM system that differs from that which is commonly presented in the study of this system as an active layer in an organic photovoltaic device. Most remarkably, the 10%, 15%, and 20% samples appear to consist of pure P3HT crystals that are dispersed in a matrix that is a homogeneous mixture of amorphous P3HT and amorphous PCBM. Further self-consistent quantitative analysis of the scattering curves provides additional validation of this model. Because the scattering curves presented here are in absolute intensity, it is possible to confirm this model by fitting the experimentally determined structure factor to the scattering of a structure/shape dispersed in a homogeneous matrix. This fitting procedure results in two crucial characteristics of the scattering particle, its size and shape, as well as the scattering length density contrast (SLDC) that exists between the scattering particle (P3HT crystal) and the matrix (amorphous mixture of P3HT and PCBM). The neutron scattering contrast between the P3HT crystal and amorphous matrix can be estimated *a priori* and compared to the values that emerge from the fitting of the experimental scattering curve to a predefined structure to provide a self-consistent check of the validity of this model.

With this goal in mind, the scattering curves of the 10%, 15%, and 20% samples that were annealed for 60 min at 150 °C were fit to an elliptical cylinder,[32] with the results presented in Figure 7. This figure shows excellent agreement between the experimentally determined structure factor and the elliptical cylinder model. More importantly, this fit is *quantitatively* consistent with the model presented above. Application of the Scherrer equation[33] on the P3HT crystal peak indicates that the crystals are consistently 84–88 Å thick, while the fits to the elliptical cylinder indicate that the P3HT crystals are 72–86 Å thick. Moreover, the experimental and model neutron scattering contrast match very well. The estimation of the scattering length density contrast of the model is detailed in the Supporting Information and depends on percent crystallinity of the P3HT, the exact density of the crystalline P3HT, amorphous P3HT, and amorphous PCBM. Because some of these values are not accurately known, the model scattering length density contrast can be estimated only within a narrow range for the model. Regardless of this limitation, this analysis provides significant insight into the validity of the proposed structure.

As listed in Table 5, the calculated SLDC of the 10% sample ranges from 0.24×10^{-6} to 0.52×10^{-6} Å^{-2}, while the sample exhibits a contrast of 0.44×10^{-6} Å^{-2}. The calculation shows that the 15% sample should exhibit a contrast of 0.41×10^{-6} to 0.78×10^{-6} Å^{-2}, while the sample has a contrast of 0.59×10^{-6} Å^{-2}, exhibiting a strong correlation between the experimentally obtained data and that of the model of a P3HT crystal in an amorphous mixture of PCBM and P3HT. The 20% sample shows poorer correlation, where the calculation predicts an SLD contrast of 0.66×10^{-6} to 1.1×10^{-6} Å^{-2}, while the analysis indicates a contrast

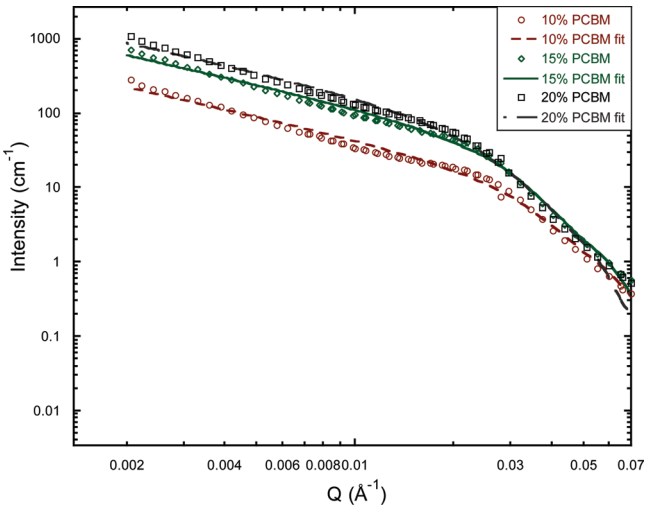

Figure 7. Fit of the structure factor of the PCBM10, PCBM15, and PCBM20 samples to the scattering of an elliptical cylinder, which models the lamellar structure of the P3HT crystals. Parameters extracted from these fits are given in Table 5.

TABLE 5. Scattering Length Density Contrast (SLDC) and Crystal Thickness Obtained from Fitting the Samples That Were Annealed for 60 min at 150 °C to an Elliptical Cylinder Model Compared to the Expected Scattering Length Density Contrast from the Model and the Crystal Size As Determined from Scherrer Analysis of the P3HT Crystalline Peak

sample	SLDC ($\times 10^6$ Å^{-2}) (model)	SLDC ($\times 10^6$ Å^{-2}) (experimental)	crystal size (exptl fit) (Å)	crystal size (Scherrer analysis) (Å)
10% PCBM	0.24—0.52	0.44	72	88
15% PCBM	0.41—0.78	0.59	82	87
20% PCBM	0.66—1.1	0.62	86	84

of 0.62 $\times$ 10^{-6} Å^{-2}. This could be explained by a lower P3HT crystallinity in this sample, but is also consistent with the interpretation that the 20% sample does not incorporate all of the PCBM into the amorphous phase due to incipient phase separation. This quantitative analysis, however, clearly shows that the 10% and 15% PCBM samples consist of pure P3HT crystals that are surrounded by an amorphous matrix that is a homogeneous mixture of amorphous P3HT and amorphous PCBM, in agreement with the model and analysis presented above.

Therefore, the qualitative and quantitative analysis of the structure factor determined by neutron scattering of P3HT/PCBM mixtures offers unprecedented insight into the thermodynamics and structure of these bulk heterojunctions. The presented results and analyses clearly show that in all samples P3HT forms crystals that exclude PCBM, and the crystals are between 120 and 150 Å in size. For the 10%, 15%, and 20% samples, the matrix surrounding these crystals is a miscible amorphous mixture of P3HT and PCBM. This is consistent with recently reported studies that demonstrate considerable miscibility of P3HT and PCBM.[34−36] It should be emphasized that the precise miscibility limit of PCBM and P3HT is not defined in these experiments, but the data indicate that it is in the vicinity of 20 vol %. The 50% PCBM sample exhibits scattering that is indicative of large-scale structure formation, signifying macroscopic phase separation. PCBM crystals are also formed in this system in these thick film (~1 mm) composites. The PCBM50 sample also forms a broad interface upon casting that becomes less sharp with thermal annealing, a result that is consistent with the mixing of the two phases upon heating.

DISCUSSION

The morphology of the active layer in OPV devices is crucial for their photovoltaic performance. The excitons must have a pathway to dissociate efficiently at an interface, and sufficient conduits for charge transport to the electrodes are also required. P3HT crystals are professed to be the primary hole carrier and thus are essential for effective charge transport. With this in mind, the ideal morphology for an organic photovoltaic is often presented as a bicontinuous, interpenetrating network morphology composed of neat P3HT and neat PCBM phases, with both phases ~200 Å in size.[1,37] Moreover, many efforts have used this model to design studies that examine the effect of the chemical structure of conjugated polymer, composition, and processing methods on the ability to achieve this ideal interpenetrating two-phase system.[14,16] However, due to limitations in contrast, the precise composition of phases, interfacial structure, and morphology of bulk heterojunctions is still unknown. For instance in electron-based techniques, crystalline P3HT and PCBM may offer sufficient

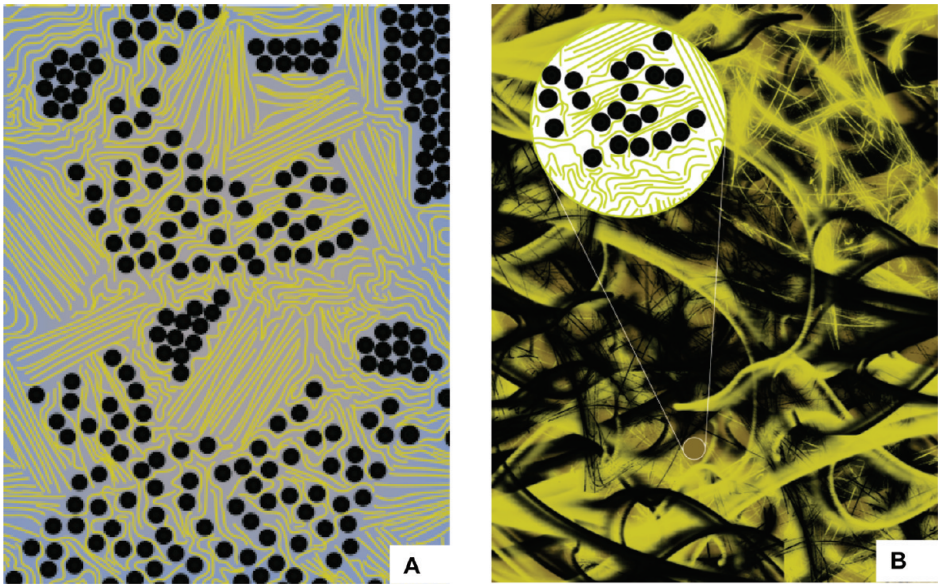

Figure 8. (A) Diagram showing the local structure of P3HT:PCBM mixtures according to the results presented here. Straight lines indicate P3HT crystalline domains, while curved lines indicate P3HT amorphous domains. Note the miscibility of PCBM in the amorphous domains, as well as pure PCBM domains. (B) Larger scale view of the P3HT:PCBM "rivers and streams" model, where the gold denotes P3HT crystals and the black denotes the pure PCBM phase, both of which are separated by a miscible phase of amorphous P3HT and PCBM, shown in brown.

contrast between those two phases; however their amorphous counterparts are almost indistinguishable. Therefore, in this work, we exploit the natural contrast of P3HT and PCBM using neutrons to provide heretofore unavailable information concerning the structure and thermodynamics of this archetypal bulk heterojunction.

It is important to note that our samples are about 1 mm, far thicker than most spin-coated samples employed as OPV active layers and many previous studies. As our samples are formed from solvent casting, they will not precisely mimic the thinner layer samples found in OPV devices. For instance the effect of confinement and the importance of the specific chemistry of the surface on the concentration distribution of the mixture are absent in our system. This is important, as it appears that confinement inhibits PCBM crystallization and PCBM crystallization is known to inhibit charge transport.[38] Therefore, one would expect that the PCBM crystallinity found in our samples will not exist in thin film active layers; however the thermodynamically driven miscibility and phase separation will remain. The relationship of this miscibility and phase separation to device performance is of utmost importance in understanding and optimizing OPV active layers.

Therefore, it is important to emphasize that the thermodynamics of this system will also control the development of structure in thinner films. We have decided to examine the problem of identifying the structure of conjugated polymer/fullerene bulk heterojunctions used in OPV cells by examining the thermodynamics and structure of the two components absent confinement. However, even in confinement, amorphous P3HT will form a miscible mixture with amorphous PCBM.[34−36] Moreover, polymers are never 100% crystalline and always contain an amorphous component, where the amorphous component is most often the majority component. Thus, *regardless of confinement* to a thin film, there will exist an amorphous phase that is a miscible mixture of P3HT and PCBM. Therefore, the results presented here provide a picture of the structure of the PCBM/P3HT active layer and provide fundamental information that is inconsistent with the model morphology of two pure interconnected, bicontinuous phases that are ~200 Å in size.

Our SANS results indicate that P3HT and PCBM form homogeneous mixtures up to ~20 vol % PCBM. The system that is more representative of that which is used as an active layer in organic photovoltaics is PCBM50, where neutron scattering shows that there exist at least three coexisting phases; P3HT crystals, a pure PCBM phase, and a mixture of amorphous PCBM and P3HT that serves as the surrounding matrix. Figure 8A shows a schematic picture of the local morphology of these 50% samples. In this picture, the yellow represent P3HT chains, and the black spheres represent PCBM molecules. Figure 8B provides a larger scale picture of the 50% sample, where the gold domains depict P3HT crystals, the black phase denotes the pure PCBM phase, both of which are separated by an amorphous mixture of P3HT and PCBM, denoted in brown.

At first, this picture may be counterintuitive, as the PCBM dispersed in the amorphous matrix must allow

charge transport throughout the sample for efficient photovoltaic activity. If not, the individual PCBM molecules will act as charge traps, decreasing PV efficiency. A simple geometric calculation, however, indicates that the PCBM molecules in the amorphous phase will be sufficiently close to allow charge transport: the distance between homogeneously dispersed spheres in a matrix, H, can be estimated from $H/D = (\Phi_m/\Phi)^{1/3} - 1$,[39] where D is the particle diameter (7 Å for C_{60})[40] and Φ_m is the maximum random packing fraction (~0.64). The result of this calculation indicates that the distance between PCBM molecules is *ca.* 4.3 Å at Φ = 15% loading and *ca.* 3.3 Å at Φ = 20% fullerene, distances that are consistent with intermolecular charge transport.

Inspection of the correlation peak and corresponding long period of P3HT crystals provide further insight into the morphology. Figure 3B and Table 2 indicate that the P3HT crystal long period in PCBM50 is similar to that of PCBM15, demonstrating that the PCBM crystals do not form between P3HT crystal domains, as, if this occurred, the long period of the P3HT would increase from 20% PCBM to 50% PCBM. On the other hand, the correlation peak is seriously distorted, suggesting that the degree of order in P3HT crystals is weakened, possibly because of the existence of PCBM crystals. It is important to emphasize that this illustration is meant to aid the reader to envision this new morphology, but is not meant to define the precise connectivity or relative sizes of the phases. Recent results[41] indicate that the pure P3HT phase forms a three-dimensional interconnected network, which is not inconsistent with the proposed morphological model.

The significant difference in neutron scattering length density of these two phases creates a clear SANS pattern that can be analyzed to provide information on the interface and crystal structure. Interestingly, the extent of P3HT crystallinity did not significantly change with thermal annealing, as has been previously reported.[42] This discrepancy can be explained by the difference in sample preparation techniques, drop casting *verus* spin coating, where drop casting allows the sample to crystallize during fabrication more than spin-coating.

The impact of these results on our understanding of the ideal morphology for photovoltaic activity is remarkable. It is clear that P3HT and PCBM do not form a bicontinuous, interconnected two-phase structure with both phases that are ~200 Å, as is currently believed. It is clear that the PCBM homogeneously disperses in amorphous P3HT up to 15−20% loadings. At all loadings, the resultant matrix also contains pure (crystalline) P3HT. At higher PCBM loadings, excess PCBM phase separates to form larger domains. The correlation of this proposed morphology with reported photovoltaic efficiencies of P3HT/PCBM samples must also be explained, as at first glance, one would expect that the amorphous PCBM/P3HT mixture would create multiple charge traps, severely limiting charge transport in this phase. However, a straightforward calculation shows that the fullerenes are sufficiently close-packed in the amorphous phase to allow charge transport, verifying the ability of this morphology to create significant photocurrent when illuminated.

We term this new model morphology "rivers and streams", as the PCBM/P3HT amorphous matrix contains an abundance of donor/acceptor interfaces resulting in the efficient dissociation of excitons into electrons and holes. These charges then "flow" in the streams of PCBM or P3HT *within* the amorphous phase to the larger pure PCBM (electrons) or P3HT (holes) phases, which act as "rivers" to transport the charges to the electrodes. This efficiency is realized only because of the extended miscibility of PCBM in P3HT, which is required to create sufficient close packing in the amorphous phase to allow charge transport in the "streams". This proposed mechanism also explains the large difference in efficiency between P3HT/C_{60} and P3HT/PCBM bulk heterojunctions, where the immiscibility of C_{60} in P3HT presumably inhibits the formation of a morphology that allows effective charge transport to the "rivers".[43,44]

CONCLUSIONS

Blends of PCBM and P3HT with varying composition were examined using small-angle neutron scattering. The effects of composition and thermal annealing at 150 °C on the resultant morphology and interfacial structure were studied. The SANS results indicate that PCBM is miscible in P3HT up to ~20 vol % PCBM, exhibiting a morphology consisting of crystalline P3HT dispersed in a miscible mixture of amorphous P3HT and PCBM. The 50 vol % PCBM sample, which models optimal photovoltaic active layers, forms a more complicated morphology that contains at least P3HT crystals, PCBM crystals, and the miscible mixture of their amorphous phases. The 10 and 15 vol % PCBM samples retain the initial morphology while annealing at 150 °C up to 6 h; however, the 20 vol % PCBM forms large-scale structures when annealed for 6 h at 150 °C, which is consistent with the onset of phase separation. Moreover, Porod analysis shows that the 50 vol % PCBM sample indicates that the interface broadens upon heating the as-cast sample, indicative of mixing.

The overarching conclusion of these studies therefore is that the morphology of the P3HT/PCBM bulk heterojunction is very different than that which is commonly reported in the literature. The extensive miscibility of the electron donor and acceptor requires

a paradigm shift in the definition of an optimal morphology in organic photovoltaics, and we propose one such morphology, "rivers and streams", that is consistent with the results of this study and the previously reported photovoltaic activity of P3HT and PCBM bulk heterojunctions.

EXPERIMENTAL METHODS

Materials. [6,6]-Phenyl-C_{61}-butyric acid methyl ester (PCBM, >99.5%) was purchased from Sigma-Aldrich, and the regioregular poly(3-hexylthiophene) (P3HT), $M_n = 64\,000$ g/mol, was synthesized by Rieke Metals and purchased from Sigma-Aldrich (Figure 1B). Both are used without further purification. P3HT/PCBM mixtures were produced by co-dissolving P3HT and PCBM in dichloromethane with a composition of 10 wt % total solids. Solutions were then deposited dropwise on a gently heated (*ca.* 110 °C) 11 mm diameter quartz disk window to accelerate drying. This procedure yielded solid disks around 1 mm thick on top of quartz windows.

Small-Angle Neutron Scattering. The SANS experiments were completed on the General Purpose SANS instrument at the High Flux Isotope Reactor at the Oak Ridge National Laboratory. Two neutron wavelengths of 4.75 and 12 Å and three sample-to-detector distances of 0.3, 8, and 18.5 m were utilized to provide Q-values ranging from 0.0012 to 0.8632 $Å^{-1}$, where $Q = 4\pi/\lambda \sin \theta/2$; λ is the neutron wavelength and θ is the scattering angle. To study the impact of thermal annealing on the morphology and interfacial structure, the structure factors of these mixtures were measured as a function of annealing time at 150 °C. The raw data were corrected for scattering from the empty cell, detector dark current, and detector sensitivity. The corrected data were then normalized to an absolute scale using a Porasil-A standard. By evaluating the slope of IQ^4 *versus* Q plots at high Q, the contribution from incoherent scattering and thermal density fluctuation is eliminated, yielding the absolute coherent scattering.

Acknowledgment. The authors wish to acknowledge the Sustainable Energy Education Research Center and the Joint Institute for Neutron Sciences at the University of Tennessee, as well as the National Science Foundation (DMR-1005987), for support of this project. We also acknowledge the support of the Scientific User Facilities Division, Office of Basic Energy Sciences, U.S. Department of Energy, who sponsors the Oak Ridge National Laboratory's High Flux Isotope Reactor. We also would like to thank W.-l. Wu (NIST) for very valuable discussions regarding the analysis of the scattering patterns and C. H. Dadmun for her help in designing and producing Figure 8.

Supporting Information Available: Estimation of the scattering length density contrast of samples, the scattering pattern of pure P3HT, the Lorentz-corrected scattering patterns of the as-cast films, a plot of $\ln(IQ^4)$ *vs* Q^2, and the Invariant plot are provided. This material is available free of charge *via* the Internet at http://pubs.acs.org.

REFERENCES AND NOTES

1. Yu, G.; Gao, J.; Hummelen, J. C.; Wudl, F.; Heeger, A. J. Polymer photovoltaic cells: enhanced efficiencies via a network of internal donor-acceptor heterojunctions. *Science* **1995**, *270*), 1789–1791.
2. Peet, J.; Kim, J. Y.; Coates, N. E.; Ma, W. L.; Moses, D.; Heeger, A. J.; Bazan, G. C. Efficiency enhancement in low-bandgap polymer solar cells by processing with alkane dithiols. *Nat. Mater.* **2007**, *6*), 497–500.
3. Ma, W. L.; Yang, C. Y.; Gong, X.; Lee, K.; Heeger, A. J. Thermally stable, efficient polymer solar cells with nanoscale control of the interpenetrating network morphology. *Adv. Funct. Mater.* **2005**, *15*), 1617–1622.
4. Li, G.; Shrotriya, V.; Yao, Y.; Huang, J. S.; Yang, Y. Manipulating regioregular poly(3-hexylthiophene): 6,6-phenyl-C-61-butyric acid methyl ester blends—route towards high efficiency polymer solar cells. *J. Mater. Chem.* **2007**, *17*), 3126–3140.
5. Li, G.; Shrotriya, V.; Huang, J. S.; Yao, Y.; Moriarty, T.; Emery, K.; Yang, Y. High-efficiency solution processable polymer photovoltaic cells by self-organization of polymer blends. *Nat. Mater.* **2005**, *4*), 864–868.
6. Kiel, J. W.; Kirby, B. J.; Majkrzak, C. F.; Maranville, B. B.; Mackay, M. E. Nanoparticle concentration profile in polymer-based solar cells. *Soft Matter* **2010**, *6*), 641–646.
7. Günes, S.; Neugebauer, H.; Sariciftci, N. S. Conjugated polymer-based organic solar cells. *Chem. Rev.* **2007**, *107*), 1324–1338.
8. Brabec, C. J.; Sariciftci, N. S.; Hummelen, J. C. Plastic Solar Cells. *Adv. Funct. Mater.* **2001**, *11*), 15–26.
9. Pivrikas, A.; Sariciftci, N. S.; Juška, G.; Österbacka, R. A review of charge transport and recombination in polymer/fullerene organic solar cells. *Prog. Photovoltaics* **2007**, *15*), 677–696.
10. Peumans, P.; Yakimov, A.; Forrest, S. R. Small molecular weight organic thin-film photodetectors and solar cells. *J. Appl. Phys.* **2003**, *93*), 3693–3723.
11. Brabec, C. J.; Cravino, A.; Meissner, D.; Sariciftci, N. S.; Fromherz, T.; Rispens, M. T.; Sanchez, L.; Hummelen, J. C. Origin of the Open Circuit Voltage of Plastic Solar Cells. *Adv. Funct. Mater.* **2001**, *11*), 374–380.
12. Park, S. H.; Roy, A.; Beaupre, S.; Cho, S.; Coates, N.; Moon, J. S.; Moses, D.; Leclerc, M.; Lee, K.; Heeger, A. J. Bulk heterojunction solar cells with internal quantum efficiency approaching 100%. *Nat. Photonics* **2009**, *3*), 297–U5.
13. van Bavel, S. S.; Bärenklau, M.; de With, G.; Hoppe, H.; Loos, J. P3HT/PCBM bulk heterojunction solar cells: impact of blend composition and 3D morphology on device performance. *Adv. Funct. Mater.* **2010**, *20*), 1458–1463.
14. Radbeh, R.; *et al*. Nanoscale control of the network morphology of high efficiency polymer fullerene solar cells by the use of high material concentration in the liquid phase. *Nanotechnology* **2010**, *21*), 035201.
15. Liu, J.; Shao, S.; Wang, H.; Zhao, K.; Xue, L.; Gao, X.; Xie, Z.; Han, Y. The mechanisms for introduction of n-dodecylthiol to modify the P3HT/PCBM morphology. *Org. Electron.* **2010**, *11*), 775–783.
16. Li, L.; Lu, G.; Yang, X. Improving performance of polymer photovoltaic devices using an annealing-free approach via construction of ordered aggregates in solution. *J. Mater. Chem.* **2008**, *18*), 1984–1990.
17. Motaung, D.; Malgas, G.; Arendse, C.; Mavundla, S.; Oliphant, C.; Knoesen, D. The influence of thermal annealing on the morphology and structural properties of a conjugated polymer in blends with an organic acceptor material. *J. Mater. Sci.* **2009**, *44*), 3192–3197.
18. Li, G.; Yao, Y.; Yang, H.; Shrotriya, V.; Yang, G.; Yang, Y. "Solvent annealing" effect in polymer solar cells based on poly(3-hexylthiophene) and methanofullerenes. *Adv. Funct. Mater.* **2007**, *17*), 1636–1644.
19. Kim, H. J.; Lee, H. H.; Kim, J. J. Real time investigation of the interface between a P3HT:PCBM layer and an Al electrode during thermal annealing. *Macromol. Rapid Commun.* **2009**, *30*), 1269–1273.
20. Campoy-Quiles, M.; Ferenczi, T.; Agostinelli, T.; Etchegoin, P. G.; Kim, Y.; Anthopoulos, T. D.; Stavrinou, P. N.; Bradley, D. D. C.; Nelson, J. Morphology evolution via self-organization and lateral and vertical diffusion in polymer:fullerene solar cell blends. *Nat. Mater.* **2008**, *7*), 158–164.
21. Ma, W.; Yang, C.; Heeger, A. Spatial Fourier-transform analysis of the morphology of bulk heterojunction materials used in "plastic" solar cells. *Adv. Mater.* **2007**, *19*), 1387–1390.

22. Brinkmann, M.; Wittmann, J. C. Orientation of regioregular poly(3-hexylthiophene) by directional solidification: a simple method to reveal the semicrystalline structure of a conjugated polymer. *Adv. Mater.* **2006**, *18*), 860–863.
23. Kim, J. Y.; Frisbie, C. D. Correlation of phase behavior and charge transport in conjugated polymer/fullerene blends. *J. Phys. Chem. C* **2008**, *112*), 17726–17736.
24. Chiu, M. Y.; Jeng, U. S.; Su, C. H.; Liang, K. S.; Wei, K. H. Simultaneous use of small- and wide-angle X-ray techniques to analyze nanometerscale phase separation in polymer heterojunction solar cells. *Adv. Mater.* **2008**, *20*), 2573–2578.
25. Watts, B.; Belcher, W. J.; Thomsen, L.; Ade, H.; Dastoor, P. C. A quantitative study of PCBM diffusion during annealing of P3HT:PCBM blend films. *Macromolecules* **2009**, *42*), 8392–8397.
26. Swinnen, A.; Haeldermans, I.; vandeVen, M.; D'Haen, J.; Vanhoyland, G.; Aresu, S.; D'Olieslaeger, M.; Manca, J. Tuning the dimensions of C60-based needlelike crystals in blended thin films. *Adv. Funct. Mater.* **2006**, *16*), 760–765.
27. Russell, T. P.; Ito, H.; Wignall, G. D. Neutron and x-ray scattering studies on semicrystalline polymer blends. *Macromolecules* **1988**, *21*), 1703–1709.
28. Mehta, R.; Dadmun, M. D. Small angle neutron scattering studies on miscible blends of poly(styrene-ran-vinyl phenol) with liquid crystalline polyurethane. *Macromolecules* **2006**, *39*), 8799–8807.
29. Debye, P.; Bueche, A. M. Scattering by an inhomogeneous solid. *J. Appl. Phys.* **1949**, *20*), 518–525.
30. Ruland, W. Small-angle scattering of two-phase systems: determination and significance of systematic deviations from Porod's law. *J. Appl. Crystallogr.* **1971**, *4*), 70–73.
31. Roe, R.-J. *Methods of X-ray and Neutron Scattering in Polymer Science*; Oxford University Press: New York, 2000.
32. Kline, S. Reduction and analysis of SANS and USANS data using IGOR Pro. *J. Appl. Crystallogr.* **2006**, *39*), 895–900.
33. Patterson, A. L. The Scherrer formula for x-ray particle size determination. *Phys. Rev.* **1939**, *56*), 978–982.
34. Treat, N. D.; Brady, M. A.; Smith, G.; Toney, M. F.; Kramer, E. J.; Hawker, C. J.; Chabinyc, M. L. Interdiffusion of PCBM and P3HT reveals miscibility in a photovoltaically active blend. *Adv. Energy Mater.* **2011**, *1*), 82–89.
35. Collins, B. A.; Gann, E.; Guignard, L.; He, X.; McNeill, C. R.; Ade, H. Molecular miscibility of polymer−fullerene blends. *J. Phys. Chem. Lett.* **2010**, *1*), 3160–3166.
36. Chen, D.; Nakahara, A.; Wei, D.; Nordlund, D.; Russell, T. P. P3HT/PCBM bulk heterojunction organic photovoltaics: correlating efficiency and morphology. *Nano Lett.* **2010**, *11*), 561–567.
37. Yang, X.; Loos, J. Toward high-performance polymer solar cells: the importance of morphology control. *Macromolecules* **2007**, *40*), 1353–1362.
38. Yang, X.; Alexeev, A.; Michels, M. A. J.; Loos, J. Effect of spatial confinement on the morphology evolution of thin poly(p-phenylenevinylene)/methanofullerene composite films. *Macromolecules* **2005**, *38*), 4289–4295.
39. Mackay, M. E.; Dao, T. T.; Tuteja, A.; Ho, D. L.; Van Horn, B.; Kim, H. C.; Hawker, C. J. Nanoscale effects leading to non-Einstein-like decrease in viscosity. *Nat. Mater.* **2003**, *2*), 762–766.
40. Melnichenko, Y. B.; Wignall, G. D.; Compton, R. N.; Bakale, G. Characterization of fullerenes and fullerene derivatives by small-angle neutron scattering and transmission measurements. *J. Chem. Phys.* **1999**, *111*), 4724–4728.
41. van Bavel, S. S.; Sourty, E.; de With, G.; Loos, J. Three-dimensional nanoscale organization of bulk heterojunction polymer solar cells. *Nano Lett.* **2009**, *9*), 507–513.
42. Shin, M.; Kim, H.; Park, J.; Nam, S.; Heo, K.; Ree, M.; Ha, C. S.; Kim, Y. Abrupt morphology change upon thermal annealing in poly(3-hexylthiophene)/soluble fullerene blend films for polymer solar cells. *Adv. Funct. Mater.* **2010**, *20*), 748–754.
43. Hoppe, H.; Sariciftci, N. S. Morphology of polymer/fullerene bulk heterojunction solar cells. *J. Mater. Chem.* **2006**, *16*), 45–61.
44. Lu, G. H.; Li, L. G.; Yang, X. N. Creating a uniform distribution of fullerene C-60 nanorods in a polymer matrix and its photovoltaic applications. *Small* **2008**, *4*), 601–606.